Desalination 563 (2023) 116730

Contents lists available at ScienceDirect

Desalination

journal homepage: www.elsevier.com/locate/desal

Plasmonic nanofillers-enabled solar membrane crystallization for mineral recovery

Sergio Santoro [a], Marco Aquino [a], Carlo Rizza [b], Anna Cupolillo [c], Danil W. Boukhvalov [d,e], Gianluca D'Olimpio [b], Shir Abramovich [f], Amit Agarwal [g], Maya Bar Sadan [f,h], Antonio Politano [b,*], Efrem Curcio [a,i,**]

[a] Department of Environmental Engineering, University of Calabria, Via Pietro Bucci Cubo 44A, 87036 Rende, CS, Italy
[b] Department of Physical and Chemical Sciences, University of L'Aquila, 67100 L'Aquila, Italy
[c] Department of Physics, University of Calabria, Via P. Bucci cube 31/C, 87036 Rende, CS, Italy
[d] College of Science, Institute of Materials Physics and Chemistry, Nanjing Forestry University, Nanjing 210037, PR China
[e] Institute of Physics and Technology, Ural Federal University, Mira 19 Str., Yekaterinburg 620002, Russia
[f] Department of Chemistry, Ben-Gurion University, Be'er Sheva 8410501, Israel
[g] Department of Physics, Indian Institute of Technology Kanpur, Kanpur 208016, India
[h] Ilse Katz Institute for Nanoscale Science and Technology, Ben Gurion University, Be'er Sheva, Israel
[i] Seligenda Membrane Technologies s.r.l., c/o University of Calabria, Via P. Bucci Cubo 45A, 87036 Rende, CS, Italy

HIGHLIGHTS

- NiSe and CoSe nanoparticles presented intense localized surface plasmons exploitable in thermoplasmonics.
- NiSe and CoSe nanofillers were immobilized on the surface of composite membranes via spray-coating.
- The photothermal effect of NiSe and CoSe boosted the vaporization of the water from brine and seawater.
- Photothermal membranes based on NiSe and CoSe nanoparticles trigger the heterogeneous crystallization of NaCl.
- Solar driven photothermal membrane crystallization intensified the salt recovery from seawater and brine.

GRAPHICAL ABSTRACT

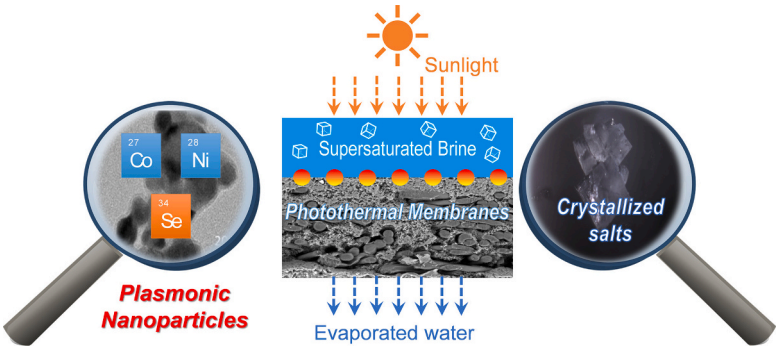

ARTICLE INFO

Keywords:
Membrane crystallization
Thermoplasmonics
Photothermal membranes
Seawater mining
Water-energy-raw materials nexus

ABSTRACT

Recently, the excitation of localized surface plasmon resonances in metal nanoparticles (NPs) has been exploited in membrane science (especially, membrane distillation) to overcome temperature polarization. However, the prohibitive costs of state-of-the-art plasmonic NPs such as Ag and Au have opened the quest of alternative materials. Here, we show that nanoscale photothermal effects activated by light irradiation on nanocomposite membranes made of a thin microporous coating of polydimethylsiloxane (PDMS) loaded with NiSe or CoSe NPs supported on polyvinylidene fluoride might be exploited to achieve crystallization of dissolved salts in brines. Explicitly, we demonstrate that the embodiment of the plasmonic NiSe and CoSe NPs is capable to originate an

* Corresponding author.
** Correspondence to: E. Curcio, Department of Environmental Engineering, University of Calabria, Via Pietro Bucci Cubo 44A, 87036 Rende, CS, Italy.
E-mail addresses: antonio.politano@univaq.it (A. Politano), efrem.curcio@unical.it (E. Curcio).

https://doi.org/10.1016/j.desal.2023.116730
Received 3 March 2023; Received in revised form 22 May 2023; Accepted 26 May 2023
Available online 1 June 2023

increase of the vaporization of the water from brine once the nanocomposite membranes are irradiated with sunlight, with the possibility to reach the supersaturation conditions, with the subsequent heterogeneous nucleation and crystallization of dissolved salts.

1. Introduction

Minerals represents a strong industrial base for the production of a wide variety of goods and services essential for the modern life, the technological progress, and the energy transition [1]. Industrial activities are strongly dependent on an adequate provision of minerals, but the supply distribution of raw materials is highly vulnerable because of the depletion of natural reserves [2,3], exacerbated by geopolitical issues [4]. Moreover, conventional extraction activities are energy-intensive practices with a strong water footprint and an adverse environmental impact [5,6].

Beyond the urgent need to implement circular strategies on mineral reuse [7], the opportunity to exploit the sea as a hypothetically unlimited mine, storing even $5{\cdot}10^{16}$ tons of minerals, has drawn attention as a potential solution to address the problem of the shortage of raw materials [8]. Moreover, the exciting new frontier of sustainable desalination is accelerating realistic significant improvements towards the valorization of hypersaline solutions (brine) rejected from seawater reverse osmosis (SWRO) plants by recovering water and minerals [9,10].

In this scenario, Membrane Distillation-Membrane Crystallization (MD-MCr) has the potential to mitigate the water-raw material nexus by recovering freshwater and dissolved salts from seawater and natural or anthropogenic brines [11–15]. MD is based on the exploitation of hydrophobic microporous membranes capable of rejecting liquid water and dissolved salts and transporting the vaporized water molecules under the action of a moderate gradient of vapor pressure across the membrane, often generated by a temperature gradient [16–18]. Being unaffected by osmotic pressure, MD allows for the protraction of the recovery of water from saline solutions up to the supersaturation (in this case, more properly denoted as MCr), finely tuning the crystallization of dissolved salts [19,20]. Interestingly, the heterogeneous nucleation of salts is governed by: (i) the precise control of supersaturation conditions modulated by the solvent evaporation rate; and (ii) the physicochemical properties of the membrane (e.g., porosity [21], roughness [22], and surface chemistry [23,24]). Unfortunately, the intrinsic heat losses, associated to the temperature polarization (TP) [25], jeopardize the energetic feasibility (100–500 $kWh{\cdot}m^{-3}$) of MD-MCr, hindering its industrial implementation [26–28]. Also in the case of the hybridization of MD-MCr with solar energy for off-grid desalination, water vaporization on membrane surface is based on inefficient “bulk” heating, entailing TP [28,29].

Definitely, the light-to-heat conversion in plasmonic NPs irradiated at their resonance frequencies can be exploited for heat harvesting in MD. Specifically, photothermal effects induce temperature increase at the boundary layer of the feed solution in contact with the membrane surface loaded with thermoplasmonic NPs [30], so as to facilitate the vaporization of the water molecules in MD experiments, thus overcoming the limitations related to the TP [30,31]. Several nanocomposite membranes showing photothermal effects were explored for photothermal MD (PhMD) applications [32]. In details, in most cases the photothermal nanofillers are noble-metal NPs (es. Au, Ag) [33,34] and carbon-based nanomaterials (es. carbon black, graphene, carbon nanotubes) [35,36].

A natural evolution of PhMD is represented by Photothermal Membrane Crystallization (PhMCr), recently validated for the self-heating graphene-based nanostructured interfaces, which have been proven to boost water evaporation upon sunlight irradiation, with the ultimate achievement of crystallization of sodium chloride (NaCl), potassium chloride (KCl), and epsomite ($MgSO_4{\cdot}7H_2O$) from brine [37]. However, the efficiency of light-to-heat conversion of graphene is peaked at infrared and ultraviolet frequencies [38]. Another implementation has been recently shown for two-dimensional nanofillers of tungsten disulfide (WS_2) embedded into polymeric membranes by phase inversion through a high-concentration functional ink, which have been exploited for the extraction of Lithium via PhMCr [39].

However, identification of plasmonic materials with resonances in the visible would be ideal for applications in PhMCr to exploit the sunlight radiation. Furthermore, such novel materials should also be compatible with an inexpensive and scalable route of synthesis to enable the massive production.

In our previous studies, we demonstrated the advantages of intensification of the desalination process by hybridization of SWRO with PhMD securing the post-treatment of the SWRO rejected brine hitting a water recovery factor of ca. 90 % obtaining a nearly saturated retentate [40,41]. Herein, this hyper-concentrated retentate generated from PhMD is valorized by PhMCr for extraction of minerals. In particular, NiSe and CoSe NPs (synthetized via solvothermal approach) have been recently demonstrated to display intense localized surface plasmons originated by the exotic quantum properties of their electronic states matching with solar radiation spectrum with potential application for desalination [41]. Herein, the superb light-to-heat conversion capability of NiSe and CoSe NPs has been used to enhance the vaporization rate of water from artificial hyper-concentrated MD brine and real seawater, securing the crystallization of NaCl, thus demonstrating the viability of plasmons-mediated seawater mining and SWRO brine valorisation.

2. Methods

2.1. Synthesis and characterization of NPs

NiSe and CoSe NPs were synthesized by solvothermal method. Firstly, nickel (II) nitrate hexahydrate $Ni(NO_3)_2{\cdot}6H_2O$ (0.2 mmol) or cobalt (II) nitrate hexahydrate $Co(NO_3)_2{\cdot}6H_2O$ (0.2 mmol) were dissolved in 50 mL of de-ionized water with stirring for 10 min, respectively. Independently, selenium powder (0.4 mmol) and hydrazine hydrate (20 mL) were stirred for 10 min. The two solutions were mixed and transferred to a Teflon-lined stainless-steel autoclave enclosing ethanolamine (10 mL) and maintained at 180 °C for 16 h. After cooling to room temperature, the achieved products were centrifuged, washed with ethanol and dried under vacuum. For Transmission Electron Microscope (TEM) experiments, suspensions were dropcasted onto a TEM grid and dried. The analyses were carried out with JEOL 2100F TEM operated at 200 kV. To check the phase, X-ray diffraction experiments were carried out using a Panalytical Empyrean powder X-ray diffractometer equipped with a position-sensitive X'Celerator detector using Cu Kα radiation.

The physicochemical properties of NiSe and CoSe NPs including their surface status were assessed by nanospectroscopy tools at the soft X-ray beamline Nanospectroscopy at Elettra-Trieste synchrotron using an energy-filtered low-energy/photo-emission electron microscope (LEEM-PEEM) microscope with spatial resolution of 10 nm.

To assess the photothermal efficacy of NiSe and CoSe, we adopt as a figure of merit the Joule number, a dimensionless parameter quantifying the NPs ability to enhance the electromagnetic field and generate heat. The Joule number was introduced by Baffou and coworkers [42] to evaluate the photothermal efficacy of isotropic spherical NPs. In this case, the expression of the heat source density q within the NP is:

$$q = \frac{\omega}{2} Im\ \varepsilon_{in} \left| \frac{3\ \varepsilon_e}{\varepsilon_{in} + 2\ \varepsilon_e} \right|^2 |\boldsymbol{E}_0|^2, \quad (1)$$

where ε_{in} is the complex dielectric permittivity of the NP and, moreover, it is considered that the NP (embedded in a uniform isotropic surrounding medium of dielectric constant ε_e) is illuminated by a monochromatic light characterized by the electric field:

$$\boldsymbol{E}(\boldsymbol{r},t) = Re\left[\boldsymbol{E}_0(\boldsymbol{r})\, e^{-i\omega t}\right] \tag{2}$$

Note that Eq. (1) holds in the long-wavelength limit, i.e., in the regime where the NP radius is smaller than the radiation wavelength. Thus, following the approach in Ref. [42], it is quite natural to define the Joule number by quantifying the photothermal efficacy as

$$J = \frac{\omega}{n_e \omega_{ref}} Im\ \varepsilon_{in} \left| \frac{3\ \varepsilon_e}{\varepsilon_{in} + 2\ \varepsilon_e} \right|^2, \tag{3}$$

where n_e is the refractive index of the surrounding medium and $\omega_{ref} = 1\ eV$. The dimensionless parameter J can be used as a figure of merit to merely compare the photothermal efficacy of plasmonic materials, enabling the comparison with a different surrounding medium at a fixed light irradiance, and accounting for both the surface plasmon-based enhancement and the ability of generating heat of each material. Here, one should also consider that NiSe and CoSe are anisotropic and their electromagnetic response is characterized by two dielectric permittivity components (viz., the in-plane and out-of-plane dielectric constants ε_{xy}, ε_z, respectively [41]. To consider and quantify the impact of the optical anisotropy on the photothermal efficacy of NiSe and CoSe, we introduce the in-plane and out-of-plane Joule numbers, namely:

$$J_{xy} = \frac{\omega}{n_e \omega_{ref}} Im\ \varepsilon_{xy} \left| \frac{3\ \varepsilon_e}{\varepsilon_{xy} + 2\ \varepsilon_e} \right|^2 \tag{4.a}$$

$$J_{z} = \frac{\omega}{n_e \omega_{ref}} Im\ \varepsilon_{z} \left| \frac{3\ \varepsilon_e}{\varepsilon_{z} + 2\ \varepsilon_e} \right|^2. \tag{4.b}$$

2.2. Membrane preparation

Polydimethylsiloxane (PDMS) from Sigma Aldrich (Italy) at a concentration of 5 wt% was solubilized in heptane from Sigma Aldrich (Italy) under magnetically stirring (400 rpm at room temperature for 3 h).

In the case of photothermal coatings, NiSe and CoSe NPs were previously dispersed in heptane by Sigma Aldrich (Italy) via sonication (Sonica®2200ETH, Soltec, Italy) for 30 min. The concentration of the photothermal NPs was 2.5 wt% with respect to PDMS. Lastly, the crosslinker was added to the polymeric solution at a concentration of 10 wt% with respect to PDMS.

The silicon-based solution was sprayed on a microporous commercial Polyvinylidene fluoride (PVDF) membrane kindly supplied by GVS Spa (Italy) (trade name Fortex®, nominal pore size 0.2 μm). Then, 10 mL of the polymeric solution were transferred to an airbrush equipped with a compressor (Gocheer, model TS100BMC, China) and mounted at 3.2 cm from the membrane on a 2D positioning control system for the planar motion at a velocity 60 mm·s^{-1} (TEVO Tornado, United States) during the spray coating. The polymeric solution was sprayed three times over PVDF membrane (112 cm^2). Finally, the composite membrane was transferred in an oven at 60 °C for 60 min to promote the crosslinking of PDMS and the evaporation of the solvent.

2.3. Membrane characterization

The morphology of the developed composite membranes was inspected with a Field Emission Scanning Electron Microscope (FESEM) Gemini SEM 500 by Zeiss (Germany) at an accelerating voltage of 2 kV. For cross section inspections, membranes were frozen in liquid nitrogen and subsequently fractured.

Measurements of water contact angle (θ) on the membrane surfaces were carried out according to the sessile drop method at room temperature by CAM 200 contact angle meter from KSV Instruments LTD (Finland). The sessile drop was deposited on membrane surfaces using an automatic micro-syringe on membrane surfaces. For all membranes 5 measurements were carried out and the average value and the corresponding standard deviation was calculated.

The mean pore (r_p) and the pore size distribution were evaluated by a PMI capillary flow porometer from Porous Materials Inc. (USA) according to the wet-up/dry-up method using Fluorinert FC-40 (surface tension = 0.017 N·m^{-1}) as the wetting liquid. Data were processed by the Caprep (Porous Materials Inc., USA) software.

Membrane porosities (ε) were estimated, according to the gravimetric method, consisting in weighting the membranes with a balance (Gibertini CRISTAL 200 SMI, Italy) in dry and wet conditions. Membranes were wetted by immersion for 24 h in Fluorinert FC40 and the porosity was calculated as:

$$\varepsilon(\%) = \left\{ \frac{(Ww - Wd)/\rho_i}{(Ww - Wd)/\rho i + \frac{Wd}{\rho P}} \right\} \%; \tag{5}$$

where W_W is the weight of the wet membrane, W_d is the weight of the dry membrane, ρ_i is the Fluorinert FC40 density (1.9 g·cm^{-3}), and ρ_P is the PVDF density (1.78 g·cm^{-3}) [43]. For each membrane, 5 measurements were performed to calculate average values and standard deviations.

An InfraRed (IR) Camera model FLIR E50 BX (FLIR, USA) with a sensitivity <0.05 °C at 30 °C and a resolution of 240 × 180 pixel and spectral range from 7.5 to 13 μm was employed for the evaluation of the temperature of the membrane surface.

The developed membranes were aged for 48 h in water; then, water was analysed using a high-resolution continuum source atomic absorption spectrometer (HR-CS AAS) to estimate the eventual leak of NiSe or CoSe NPs.

2.4. Solar-driven photothermal membrane crystallization

2.4.1. Experimental studies

Experiments of solar-driven PhMCr were conducted using a hypersaline solution of NaCl 5 M, prepared by dissolving sodium chloride (VWR, Italy) in deionized water (5.5 μS·m^{-1}) produced by PURELAB (Elga LabWater, UK). Polylactic acid (PLA) membrane modules, designed with Autodesk 123D® and 3D-printed (TEVO Tornado, United States), were equipped with the photothermal membranes (active area 3.14 cm^2). The feed compartment presented a transparent window to irradiate the membrane surface. The permeate surface of the membrane was exposed to air to minimize the impact of the conductive heat transferred from the feed side on the TP. The saline feed solution was thermostated at 20 °C and fed at 10 mL·min^{-1} with micro-peristaltic pump (Reglo, Ismatec, US) (Fig. 1). Experiments of PhMCr were performed at environmental conditions (relative humidity of 47 ± 4 % and a temperature of 20.0 ± 0.5 °C) by exposing the feed membrane surface to the artificial radiation of a solar simulator (Abet Technologies, US) with irradiance of 1 sun (1000 W·m^{-2}). The evaporation rate was estimated by measuring the weight variation of the feed using an analytical balance.

The obtained crystals were collected from the feed tank by Polyethersulfone (PES) syringe filter with nominal pore size of 0.1 μm. Subsequently, they were characterized by a Zeiss microscope, model AxioLab 1× (Germany) to estimate their size. The coefficient of variation (CV) representing the dispersion of the size distribution curve around the mean size was calculated.

$$CV = \frac{L_{84\%} - L_{16\%}}{2 \cdot L_{50\%}}; \tag{6}$$

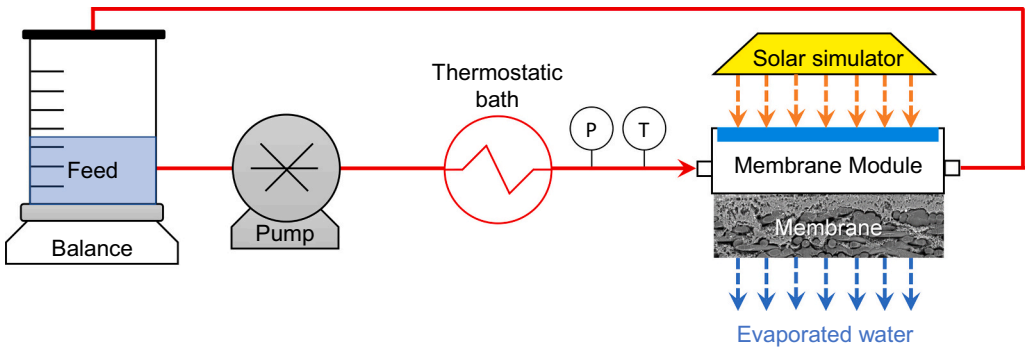

Fig. 1. Scheme of the setup employed for solar-driven Photothermal Membrane Crystallization.

where L is the crystal size taken from the F(L) curve at the indicated percentage [44].

X-ray Powder Diffraction (XRPD) analysis of the crystallized salts was performed using a Bruker D8 Advance X-Ray diffractometer (Bruker, Karlsruhe, Germany) with Bragg-Brentano geometry, with a copper sealed tube X-ray source producing Cu kα radiation (wavelength of 1.5406 Å) from a generator operating at 40 kV and 40 mA. The diffracted X-rays were recorded on a scintillation counter detector located behind a set of long Soller slits/parallel foils. Scans were collected in the range of 3–65° 2θ, using a step size of 0.014° 2θ and a step counting time of 0.2 s. EVA software (DIFFRACplus EVA version 11.0. rev. 0) was used to identify mineral phases by comparing experimental patterns with 2005 PDF2 reference patterns.

The photothermal efficiency (η_v) of the developed membranes quantifies the effectiveness of the light-to-heat-to vapor conversion and it was estimated as [45]:

$$\eta_v = \frac{J_w \cdot (\lambda_v + Q)}{P_{in}}; \tag{7}$$

where J_w is the flux of water vapor ($g \cdot m^{-2} \cdot s^{-1}$), λ_v the latent heat of vaporization of water ($J \cdot g^{-1}$), Q sensible heat of water ($J \cdot g^{-1}$), and P_{in} the power of the incident light ($W \cdot m^{-2}$), respectively.

The water evaporation flux (J_w), quantified through Eq. (8), is proportional to the difference between the vapor pressure of water at the membrane surface and the partial pressure of water vapor in air $\left(p_w^{membrane} - p_w^{air}\right)$ as follows:

$$J_w = K\left(p_w^{membrane} - p_w^{air}\right). \tag{8}$$

The role of the photothermal nanofillers is to increase the driving force of the evaporation rate by raising the value of $p_w^{membrane}$, which is dependent, according to Raoult's law, on the vapor pressure of pure water p_w^0 evaluated at the interface temperature of the irradiated membrane $\left(T_f^*\right)$, the molar fraction (x_w), and the activity coefficient (γ_w, $\neq 1$ for a non-ideal mixture) of water in the feed solution. Moreover, p_w^{air} is affected by saturated water vapor pressure (p_w^0), evaluated at the actual dry bulb temperature (T_{air}), and relative humidity (φ). Thus, J_w can be expressed as:

$$J_w = K\left[p_w^0\left(T_f^*\right) \cdot x_w \cdot \gamma_w - p_w^0(T_{air}) \cdot \frac{\varphi}{100}\right]. \tag{9}$$

To confirm the performance of the photothermal membrane in real conditions, experiments were also conducted using real seawater collected from Tyrrhenian sea in Amantea (Italy) vaporized under the natural sunlight irradiation. The saline solution was stored at 4 °C, then thermostated at room temperature for 2 h, and microfiltered through 0.20 m pore size polypropylene (PP) membranes (Microdyn®) before the experiments.

The concentration of ions solubilized in the seawater was estimated with Ion Chromatography (Metrohm 861 Advanced Compact Ion Chromatography, Switzerland) using 3.2 mM Na_2CO_3 + 1 mM $NaHCO_3$ solution as the eluent for the anion column Metrosep A Supp 5 - 250/4.0 and 2 mM nitric acid +0.25 mM oxalic acid solution for the cation column Metrosep C4 – 250/4.0.

2.4.2. Crystallization kinetics

According to the Classical Nucleation Theory (CNT), the impact of the membrane surface to facilitate the nucleation is quantified by the ratio of the Gibbs energy barrier for heterogeneous nucleation occurring at the membrane interface (ΔG_{het}^*) to the one for homogeneous nucleation occurring in the bulk of the solution (ΔG_{hom}^*), as following [21]:

$$\frac{\Delta G_{het}^*}{\Delta G_{hom}^*} = \frac{1}{4}(2 + cos\theta)(1 - cos\theta)^2\left[1 - e\frac{(1 + cos\theta)^2}{(1 - cos\theta)^2}\right]^3. \tag{10}$$

Furthermore, the CNT describes the crystallization as a thermally activated process, where the nucleation rate (B) (the number of new crystals that are generated per unit of time per unit solution volume) is correlated to ΔG^* (Gibbs energy barrier) by:

$$B = \Gamma \cdot e^{-\frac{\Delta G^*}{k_B \cdot T}}; \tag{11}$$

where Γ is the pre-exponential kinetic parameter and k_B is the Boltzmann's constant, respectively.

As described by the CNT, the nucleation rate B is associated to supersaturation S by the equation:

$$B = a \cdot exp\left(\frac{-b}{lnS^2}\right); \tag{12}$$

where a is a preexponential factor and b is a constant [46].

The growth rate (R_G) is described by the following empirical correlation:

$$R_G = k_G(c - c^*)^g; \tag{13}$$

With k_G are the kinetic rate constant, g the growth rate order, c the actual salt concentration and c^* the NaCl solubility, respectively.

3. Results

3.1. Physicochemical properties of NiSe and CoSe NPs

Using X-ray photoelectron microscopy (XPEEM), NiSe and CoSe NPs were imaged (see Fig. 2 g-h) and core levels were acquired (Fig. 2d) with nanoscale resolution. To provide information on the surface of NPs, surface sensitivity was enhanced by using low energy photons (200 eV). Specifically, we observed by m-XPS (X-ray photoelectron spectroscopy) two different oxidation states in Se-3d core levels (Fig. 2d) arising from Se(II) and Se(0) species at binding energy of 53.8 and 55.2 eV, respectively. Notably, SeO_2 species typically at BE = 58–59 eV are absent, while in previous studies on NiSe NPs their spectral component was even

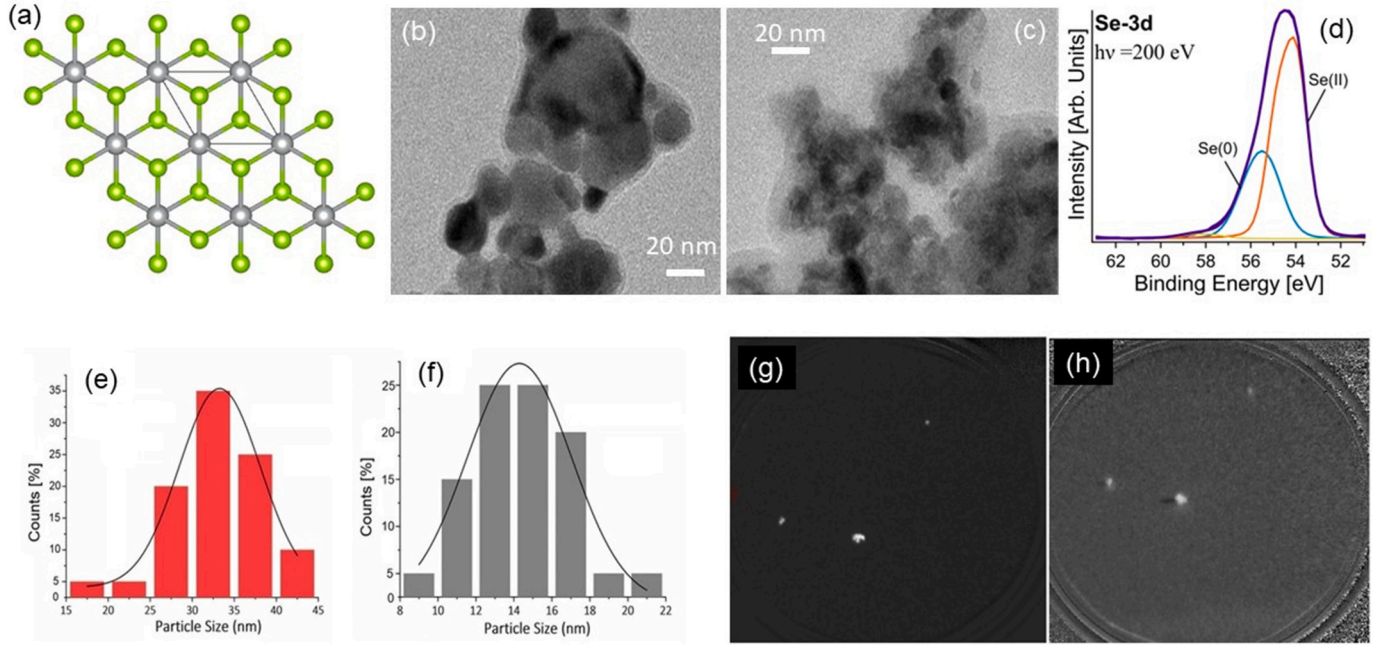

Fig. 2. (a) Atomic structure of NiSe and CoSe. Panels (b, c) report TEM images of (b) NiSe and (c) CoSe NPs. (d) μ-XPS spectrum for Se-3d on an individual NiSe NP measured by XPEEM apparatus, with a photon energy of 200 eV. Panels (e)-(f) show the histogram distribution of (e) NiSe and (f) CoSe NP size, respectively. Panels (g) and (h) show the (g) XPEEM and (h) XAS-PEEM images of NiSe NPs acquired at the energy of (g) Se-$3d_{5/2}$ and (h) Ni-L_3 absorption edge, respectively.

predominant in the region of Se-3d core levels [47]. Based on statistical analysis of several datasets of TEM images on (Fig. 2b) NiSe and (Fig. 2c) CoSe NPs, the distribution of their particle size was determined (Fig. 2e-f), finding an average diameter of 30 ± 7 nm and 15 ± 5 nm for NiSe and CoSe NPs, respectively.

3.2. Light-to-heat conversion

Fig. 3 compares the Joule numbers of NiSe and CoSe with that of silver (taken as a state-of-the-art reference for photothermal conversion). From Fig. 3, it is evident that the photothermal conversion in NiSe and CoSe is more efficient than Ag in the considered optical range. In Fig. 3, the Joule numbers of NiSe and CoSe were evaluated by Eqs. ((4.a), (4.b)), where the complex dielectric functions of NiSe and CoSe (numerically calculated through a time-dependent density functional theory [41]). The Joule number for silver obtained by Eq. (3), where the Ag dielectric constant has been evaluated by a suitable Drude-Lorentz model [48]. For the sake of simplicity we calculated Joule numbers for the case where the NPs are embedded in vacuum ($\varepsilon_e = n_e^2$=1).

3.3. Membrane characterization

The morphology of the composite membranes was revealed by SEM cross-sectional micrograph (Fig. 4a) made of a non-woven tissue impregnated by polyvinylidene fluoride (PVDF) with a thickness of 180 ± 2 μm. Energy Dispersive Spectroscopy (EDS) analyses showed that silicon is concentrated on a layer of 2 μm over a support rich of fluorine atoms. Thus, the PVDF membrane was effectively coated with a thin and porous layer of $(C_2H_6OSi)_n$ (PDMS) (Fig. 4b). In fact, the high volatility of heptane (vapor pressure of 5.3 kPa at 20 °C) combined with the nebulization of the sprayed solution secured a rapid vaporization of the solvent and the deposition of the PDMS on the membrane surface, avoiding the formation of a dense layer and/or the penetration of silicon into the pores. This enabled the localization of the photothermal nanofillers on the membrane surfaces as demonstrated by EDS analysis attesting the presence of NiSe and CoSe exclusively into the PDMS coating (Fig. 4c-d). Importantly, the morphology of composite

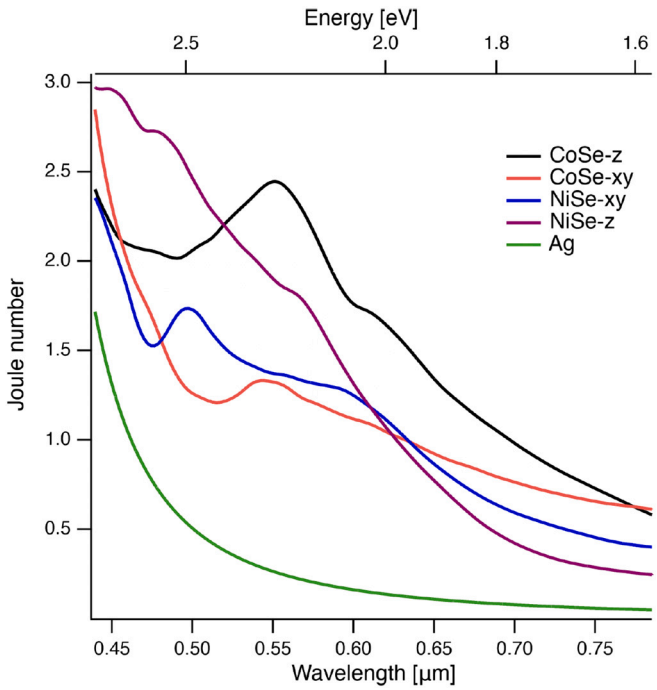

Fig. 3. Joule number of Ag, NiSe, and CoSe. In the visible range (energies from 1.6 to 3.2 eV and wavelengths from 780 to 380 nm), Ag is unquestionably less efficient in photothermal conversion than NiSe and CoSe. For NiSe and CoSe, owing to their crystal anisotropy, the xy and z contributions are distinctly accounted.

photothermal membranes guaranties the light-to-heat conversion on the thin nanocomposite coating localizing the heat harvesting at the boundary layer of the feed, while the polymeric microporous support plays a pivotal role in conferring thermal isolation and mechanical stability to the photothermal coating.

As a manner of fact, the characterization of the membranes (Table 1)

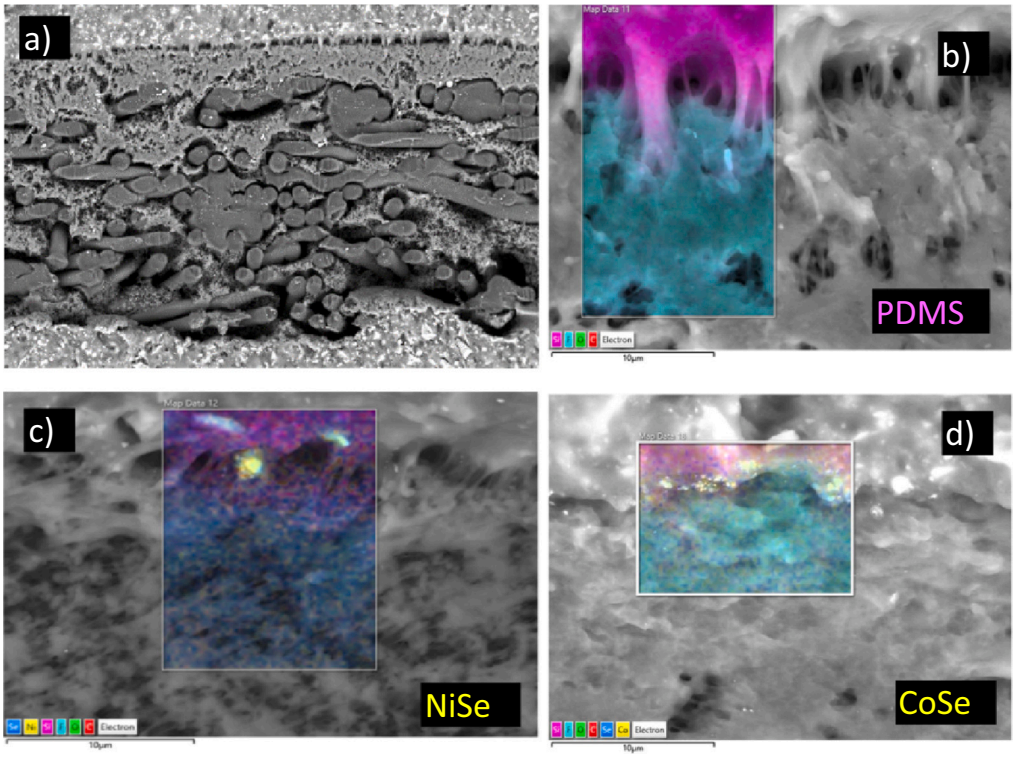

Fig. 4. (a) SEM micrographs of PDMS/PVDF membrane: cross-sectional view (magnification 900×); EDS cross-sectional analysis of composite membranes: (b) bare PDMS (denoted as "PDMS"), (c) PDMS/2.5 wt% NiSe coating (denoted as "NiSe") and (d) PDMS /2.5 wt% CoSe coating (denoted as "CoSe"). Fuchsia, cyan, and blue spots in color maps refer to Si, F and Se atoms, respectively; Ni and Co atoms glow yellow.

Table 1
Membrane characterization.

Membrane	PVDF	PDMS	NiSe	CoSe
$r_{average}$ (μm)	0,21 ± 0,01	0,20 ± 0,02	0,19 ± 0,03	0,20 ± 0,02
$r_{largest}$ (μm)	0,28 ± 0,02	0,26 ± 0,03	0,26 ± 0,03	0,24 ± 0,03
ε (%)	58,7 ± 0,7	57,1 ± 1,1	57,4 ± 0,9	58,0 ± 1,3
Θ (°)	113 ± 4	117 ± 5	122 ± 3	112 ± 4

confirmed that the PDMS and the nanocomposite coatings marginally impacted on the properties of the membranes. Explicitly, in all cases (PVDF support, PDMS/PVDF, PDMS+2.5 wt% NiSe/PVDF and PDMS+2.5 wt% CoSe/PVDF), porosity ranging from 57.1 % to 58.7 %, with a mean pore size of 0.19–0.21 m and a contact angle of 112°–122° were observed (see Table 1). Despite the hydrophilic nature of metal NPs (i.e., NiSe and CoSe), their embodiment into a highly rough PDMS coating secured to the nanocomposite surfaces a hydrophobic character necessary to avoid permeation of the liquid water (i.e., pore wetting) [49,50]. Moreover, no NiSe and CoSe NPs were detected by HR-CS AAS in the water employed for aging test, thus demonstrating the absence of leakage phenomenon of the plasmonic hotspots from the coating and confirming the thermodynamic compatibility of PDMS with NiSe and CoSe NPs [51,52].

Infrared maps of the sunlight-exposed membrane revealed the effective light-to-heat conversion enabled by plasmonic NiSe and CoSe nanofillers (Fig. 5.a). While the bare polymers (PVDF and PDMS/PVDF) reached a surface temperature in the range of 31.5 ± 0.9 °C under sunlight irradiation, the coating of PDMS embedding CoSe (2.5 wt%) NPs achieved a temperature of 61.7 ± 0.4 °C. In the case of PDMS/2.5 wt% NiSe coating, the temperature measured on the membrane surface was 51.9 ± 0.6 °C. The light-to-heat conversion provided by thermoplasmonic nanofillers facilitated the vaporization of the water under the sun irradiation. The PVDF membrane coated by PDMS showed a photothermal efficiency (η) estimated according to Eq. (7) of 18.2 %, whereas the embodiment of NiSe and CoSe NPs secured an improvement of the temperature of the membrane surface, raising the photothermal efficiency up to 37.9 % and 54.9 %, respectively (Fig. 5.b).

3.4. Photothermal membrane crystallization

3.4.1. Photothermal membrane crystallization from artificial brine

The beneficial effects of the phothothermal nanofillers are evident from the inspection of Fig. 6.a. Definitely, the higher surface temperature $\left(T_f^*\right)$, generated by the light-to-heat conversion, resulted into an exponential increase of water vapor pressure, as determined by the Clausius-Clapeyron equation. Consequently, higher evaporation fluxes (J_w) were observed. Under solar irradiation, while the bare PDMS coating assured an evaporation rate of 0.145 ± 0.025 $L{\cdot}m^{-2}{\cdot}h^{-1}$ (T_f^*=31.5 °C), the value of J_w increased to 0.445 ± 0.021 $L{\cdot}m^{-2}{\cdot}h^{-1}$, when entrapping 2.5 wt% NiSe into the PDMS coating layer (T_f^*=51.9 °C). The best performance (0.612 ± 0.08 $L{\cdot}m^{-2}{\cdot}h^{-1}$) was attained for the PDMS/CoSe coating at an interface temperature T_f^*=61.7 °C, hitting a four-fold improvement with respect to the bare PDMS (Fig. 6a). Noteworthy, the improvement of J_w is related to the suppression of the impact of the heat losses on the TP due to the thermoplasmonic activity of CoSe NPs capable of compensating both the convective heat transfer from the boundary layer to the feed bulk [53] and the latent heat of water vaporization [54]. The value of K in Eq. (9), interpolating experimental data for the tested membranes, was 4.5 ± 0.4 $L{\cdot}m^{-2}{\cdot}h^{-1}{\cdot}atm^{-1}$.

The progressive vaporization of the water increased the concentration of NaCl, leading the system towards supersaturation S (defined as the ratio of the actual salt concentration on the solubility). It is worth mentioning that the improvement of the temperature from 20 to 60 °C slightly affected the solubility (+3 %) of NaCl, that is 361 g NaCl/kg H_2O at room temperature [55]. A higher evaporation rate (J_w) resulted into a

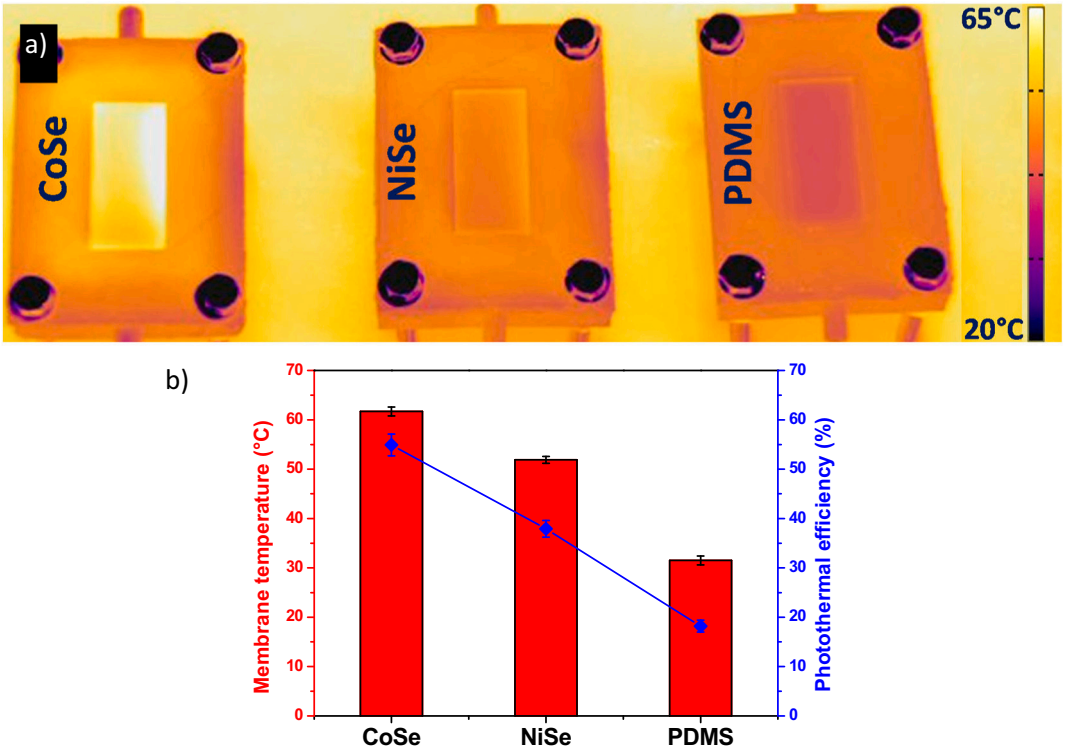

Fig. 5. (a) Infrared maps of membrane surface, (b) temperature of the membrane surface and photothermal efficiency under the exposition under solar radiation at the steady-state (after 10 min) of (i) bare PDMS coating (denoted as "PDMS"), (ii) nanocomposite coating based on 2.5 wt% of NiSe NPs embedded into PDMS (denoted as "NiSe"), and (iii) nanocomposite coating based on 2.5 wt% of CoSe NPS embedded into PDMS (denoted as "CoSe").

rapid achievement of a higher level of supersaturation, thus enhancing the nucleation rate. Coherently, NaCl crystals were visible after 45 min on the surface of the membrane loaded with CoSe, i.e., 15 min earlier than the appearance of the NaCl crystals on the surface of the silicon-based coating with NiSe nanofillers. A few of NaCl crystals appeared also on the PDMS coating after about 120 min.

After 2 h of crystallization tests, the higher supersaturation generated by PDMS/CoSe ($S = 1.6$), compared to PDMS/NiSe ($S = 1.3$) and PDMS ($S \sim 1$), resulted into a superior number of crystallized salts. In fact, the magma density collected from the surface of bare PDMS was 0.086 g of NaCl·cm^{-3} of mother liquor, raising to 0.124 g of NaCl·cm^{-3} for the nanocomposite coating loaded with 2.5 wt% of CoSe NPs.

This is consistent with the inspection of the surfaces of the coatings with the optical microscope, revealing the beneficial effects of the photothermal NPs in terms of population of NaCl crystals, as shown in Fig. 6 c-d. In fact, the higher crystal density was observed after 120 min on the surface of PDMS/2.5%wt CoSe (63 ± 3 crystals·cm^{-2}), whereas 51 ± 3 crystals·cm^{-2} were detected over PDMS/2.5%wt NiSe.

NaCl crystals grown on bare PDMS exhibited orthorhombic shape with aspect ratio of about 1.4 (Fig. 6c). In the case of PhMCr carried out with PDMS/2.5%wt NiSe and PDMS/2.5%wt CoSe (Fig. 6e), the crystals of NaCl presented a well-defined cubic shape with an aspect ratio of ca. 1.1. Moreover, the Crystal Size Distribution (CSD) of NaCl collected from both the membrane surface made of PDMS load with NiSe or CoSe presented a Gaussian distribution (Fig. 6b). After 60 min of the generation of the supersaturation conditions, NaCl crystals obtained on PDMS/2.5%wt CoSe presented a mean size of 108 ± 4 μm and a narrow size distribution (CV of 28 %); whereas NaCl crystals nucleated on PDMS/2.5%wt NiSe showed a larger size (166 ± 4 6 nm) and similar CV (33 %).

The narrow CSD of the NaCl crystals grown on photothermal composite membranes loaded with NiSe or CoSe nanofillers was attributed to the uniform supersaturation profile within the boundary layer adjacent to the photothermal membrane, where heterogeneous nucleation took place. Nevertheless, the higher surface temperature archived by the membrane doped with CoSe in comparison to PDMS/2.5%wt NiSe secured a higher rate of removal of water quickly driving the brine towards supersaturation conditions. The ultimate result is the subsequent formation of a higher number of nuclei with a lower critical size.

3.4.2. *Kinetic studies*

The crystallization of dissolved salts takes place according to two different phases: (i) nucleation and (ii) growth. While these two steps are indistinguishable in batch crystallization (homogeneous crystallization), in MCr the membrane serves as a preferential surface for the facilitated nucleation, whereas the crystals grow in the bulks (heterogeneous nucleation) [56–58]. In fact, in batch crystallization, the random movement of solutes drastically reduces the effective interactions responsible for the nucleation [59], whereas in the case of heterogeneous nucleation, the energy required to generate a critical nucleus (Gibbs energy barrier, ΔG^*) is reduced by the membrane by offering reversible chemical interactions and microenvironments, which favor the assembling of the nascent nuclei [23,59,60].

The values of $\frac{\Delta G^*_{het}}{\Delta G^*_{hom}}$ for membranes developed in this work lie in the range of 0.6 ± 0.1. Thus, the membrane surface of bare PDMS and PDMS loaded with NiSe or CoSe nanofillers facilitated the extraction of minerals by reducing ΔG^* required for NaCl crystallization.

Fig. 7a confirmed the agreement of the experimental results with the CNT showing a linear trend for the logarithm plot of the nucleation rate (B). Moreover, Eq. (11) presents an Arrhenius-like trend of B as a function of temperature T, highlighting a beneficial effect of the employment of PhMCr as an improvement of T_f^* positively affect B. In fact, the microscopic inspection of the mother liquor after 120 min revealed a value of B for the photothermal membrane loaded with CoSe NPs of 4.2 ± 0.3·10^5 #crystals·m^{-3}·s^{-1} (T_f^*=61.7 °C), higher than the value of 2.9 ± 0.2·10^5 #crystals·m^{-3}·s^{-1} observed for PDMS/2.5%wt

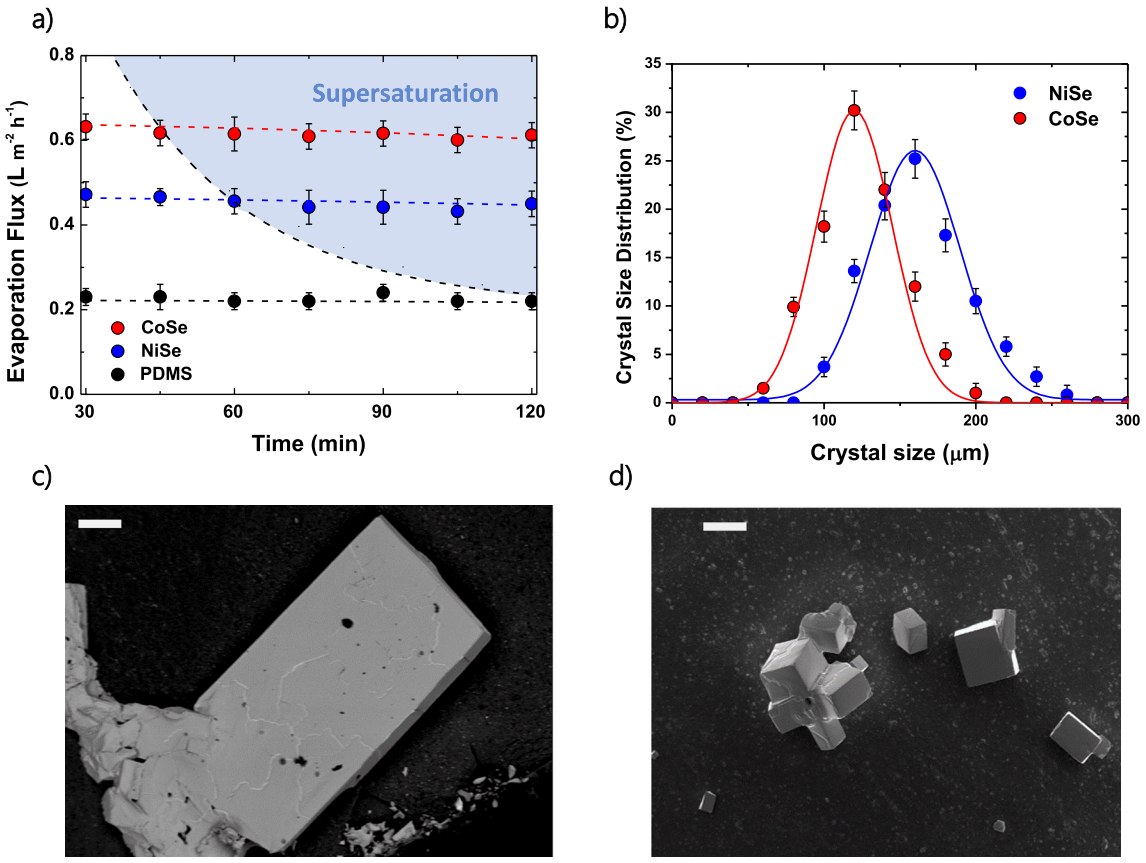

Fig. 6. (a) Evaporation flux (symbols are experimental data, dotted lines are generated by Eq. (9)) versus time for composite membranes under solar radiation; (b) Crystal size distribution (CSD) of NaCl collected on the surface of composite membranes observed 60 min after the supersaturation; (c) SEM image of NaCl crystals nucleated on the surface of bare PDMS coating; (d) SEM image of NaCl crystals nucleated on PDMS/2.5 wt% CoSe coating (scale bar: 100 μm).

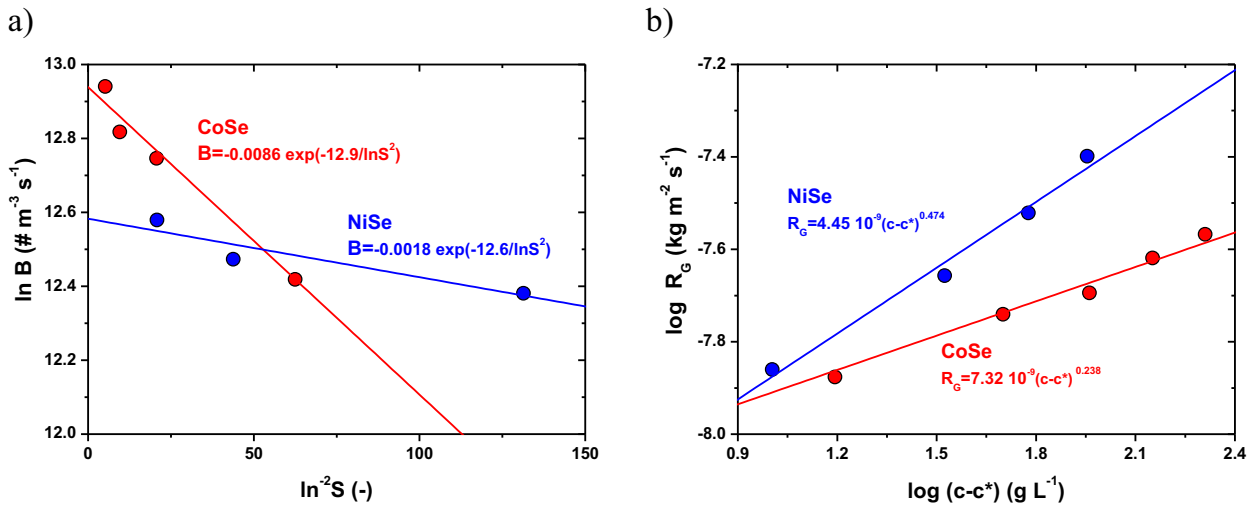

Fig. 7. Experimental results of: (a) nucleation rate vs. supersaturation and (b) mass growth rate vs. supersaturation of NaCl in experiment of PhMCr performed with PDMS/2.5 wt% NiSe and PDMS/2.5 wt% CoSe.

NiSe (T_f^*=51.9 °C). Analogously, the recovery minerals from shale gas produced by MD-MCr demonstrated values of B ranging from $2.9{\cdot}10^5$ #crystals·m^{-3}·s^{-1} to $8.2{\cdot}10^5$ #crystals·m^{-3}·s^{-1} as a function of the flow rate of the feed at a temperature of 30 °C [61].

Nevertheless, the main advantage of the employment of photothermal membranes is the intensification of the vaporization of the water (high J_w), enabling a rapid achievement of the supersaturation conditions ($S > 1$), triggering the nucleation of dissolved salts.

By plotting the logarithm values of R_G and $(c - c^*)$, experimentally estimated by sampling the mother liquor during the experiment of PhMCr, the kinetic parameters k_G and g were determined (Fig. 7b). The slope of the linear trend provided the value of g of 0.238 and 0.474 for the photothermal layer of PDMS with CoSe and NiSe nanofillers, respectively. Such values are comparable with the one observed for

conventional MCr performed on real seawater with a pilot plant equipped with 0.4 m^2 of polypropylene hollow-fibers ($g = 0.56$) [62]. Moreover, the kinetic constant k_G for PDMS/2.5%wt CoSe and PDMS/2.5%wt NiSe was estimated to be $5.98{\cdot}10^{-9}$ $kg{\cdot}m^{-2}{\cdot}s^{-1}$ and $4.45{\cdot}10^{-9}$ $kg{\cdot}m^{-2}{\cdot}s^{-1}$, higher than the value of $2.78{\cdot}10^{-9}$ $kg{\cdot}m^{-2}{\cdot}s^{-1}$ by Ji et al. [62]. The photothermal efficacy of CoSe and NiSe nanofillers included in PDMS secured a growth rate of NaCl of $1.52 \pm 0.14{\cdot}10^{-7}$ $m{\cdot}s^{-1}$ and $1.65 \pm 0.25{\cdot}10^{-7}$ $m{\cdot}s^{-1}$, respectively. For the sake of comparison, we mention that NaCl typically grows at a rate ranging from $3.5{\cdot}10^{-8}$ to $1.3{\cdot}10^{-7}$ $m{\cdot}s^{-1}$ in conventional crystallization [63].

3.4.3. Extraction of NaCl from real seawater

Experiments of PhMCr were carried out with real seawater containing Na^+, Mg^{2+}, K^+, and Ca^{2+} as major cations and Cl-, SO_4^{2-}, CO_3^-, Br-, NO_3^- as major ions (Table 2), leading to an ionic strength of 0.958 *m*.

Before the PhMCr tests, sodium bicarbonate ($NaHCO_3$) was added to seawater adjusting the CO_3/Ca molar ratio to 1.3. This step secured a significant mitigation of the risk of inorganic scaling mostly caused by calcium-based compounds since $NaHCO_3$ was found to be an effective selective agent for the removal of Ca^{2+} from seawater precipitating in forms of $CaCO_3$ or $CaSO_4$; as recently demonstrated by Molinari et al. [64].

Water evaporation fluxes from seawater under solar irradiation are consistent with those measured from artificial NaCl solutions. Again, the higher J_w was observed when entrapping 2.5 wt% CoSe into the PDMS coating layer (0.601 ± 0.012 L m^{-2} h^{-1}), whereas values of J_w of 0.4289 $\pm$ 0.016 and 0.221 ± 0.031 L m^{-2} h^{-1} were measured for PDMS/2.5%wt NiSe and bare PDMS, respectively. Consequently, the rapid concentration of the real seawater induced by the superior photothermal conversion of CoSe NPs (as already demonstrated for the NaCl solution) reduced the time required for the formation of the crystals from ca. 175 to 350 min with respect to the bare PDMS.

Beside the typical cubic shape, X-ray diffraction (XRD) confirmed the crystallization of NaCl crystals in form of halite with a purity above 99 % (Fig. 8) from real seawater. In fact, XRD patterns obtained from the salt crystallized over the surfaces of PDMS/2.5%wt NiSe and PDMS/2.5%wt CoSe presented the typical peaks of halite (27.4°, 31.7°, 45.4°, 53.7°, 56.4°) according to the Joint Committee on Powder Diffraction Standards (JCPDS). Definitively, the high content of Na^+ and Cl^- in real seawater (with a concentration of ca. one order of magnitude higher than Mg^{2+} and SO_4^{2-}, i.e., the second major cation and anion, respectively) and the pre-treatment for Ca-ions precipitation using $NaHCO_3$ are responsible for the chemical nature and the high purity of the halite crystallized via PhMCr.

4. Conclusions

The socioeconomic changes are deeply dependent on the availability of metals and minerals, but the mining sector has been widely recognized as an energy-intensive sector with a severe water footprint. Thus, the development of alternative green and sustainable technologies for the extraction of raw materials is an imperative. MCr has gained more attention as an innovative approach to intensify the selective crystallization of solutes from aqueous solution coupled with a simultaneous recovery of the water, opening the door for the exploitation of the sea as a renewable mine. Unfortunately, the high specific energy consumption has hampered the practical implementation of MCr at large scale so far.

Here we implemented a novel thermoplasmonic nanotechnology in order to intensify the evaporation rate of water and therefore the crystallization of dissolved salts by devising a PhMCr process based on the light-to-heat conversion enabled by localized surface plasmon resonances in CoSe and NiSe NPs, whose performances exceed those of state-of-the-art materials for thermoplasmonics (namely, silver) already in the first implementation.

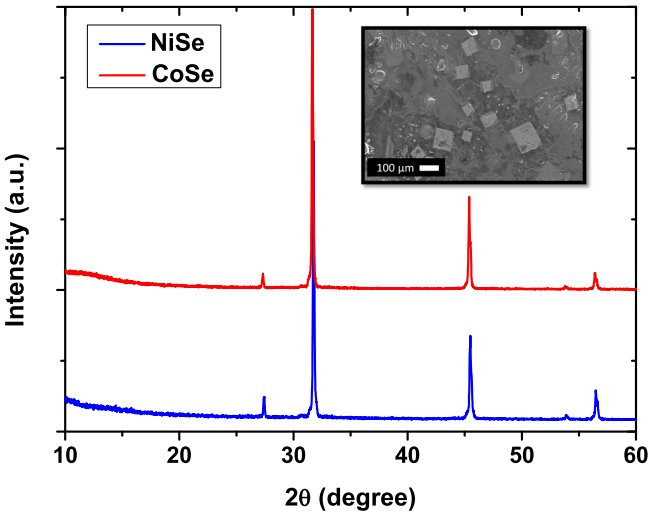

Fig. 8. XRD diffractogram of salts extracted from seawater via PhMCr with PDMS/2.5%wt NiSe and PDMS/2.5%wt CoSe. Inset: the SEM picture of crystals obtained from PDMS/2.5%wt CoSe.

NiSe and CoSe nanofillers were immobilized into microporous hydrophobic layer of ca. 2 µm of PDMS onto a PVDF membrane via spray-coating. Once irradiated with sunlight, nanocomposite membranes with NiSe and CoSe NPs were found to be able to convert the sunlight into heat with efficiency of 37.9 % and 54.9 %, respectively.

The solar-driven activated thermoplasmonic effect of NiSe and CoSe was utilized to boost the vaporization of water from NaCl brine. Explicitly, PDMS/2.5%wt CoSe reached a surface temperature of 61.7 °C boosting the evaporation flux to 0.608 $L{\cdot}m^{-2}{\cdot}h^{-1}$, 4-fold higher than the performance of bare PDMS coating (0.145 $L{\cdot}m^{-2}{\cdot}h^{-1}$ at a surface temperature of 31.5 °C). In the case of the PDMS coating embedding 2.5 wt % NiSe, the surface temperature under sunlight irradiation was 51.9 °C, resulting in a water evaporation of 0.445 $L{\cdot}m^{-2}{\cdot}h^{-1}$ from NaCl brine. Noteworthy, the rapid vaporization observed for PDMS/2.5%wt CoSe drastically reduced (by 62.5 %) the time required to get the supersaturation conditions in NaCl brine with respect to blank PVDF.

The implementation of PhMCr also provided improvements in terms of the quality of crystals. Explicitly, the homogeneous membrane surface temperature secured by the nanoscale thermal hotspots generates consistent conditions for the nucleation and the crystallization, resulting in the growth of high-quality crystals (CV of 29 % for PDMS/2.5%wt CoSe). Furthermore, kinetic studies confirmed that the higher surface temperature activated by photothermal effects facilitated the nucleation phase. Lastly, the feasibility of PhMCr was demonstrated by extracting NaCl (purity>99 %) from real seawater.

Overall, this work outlines the potentialities of PhMCr with relevant economic, energetic, and environmental impacts.

CRediT authorship contribution statement

Sergio Santoro: Conceptualization, Writing – original draft, Writing

Table 2
The ionic composition of seawater measured by ion chromatography (major ions are reported).

Ion	Na^+	Mg^{2+}	K^+	Ca^{2+}	Cl^-	SO_4^{2-}	CO_3^-	Br^-	NO_3^-
Concentration (ppm)	17,951	2118	678	490	20,821	2199	160	114	65

– review & editing, Supervision. **Marco Aquino:** Investigation, Validation, Visualization. **Carlo Rizza:** Formal analysis, Data curation. **Anna Cupolillo:** Formal analysis. **Danil W. Boukhvalov:** Validation, Formal analysis. **Gianluca D'Olimpio:** Formal analysis, Data curation. **Shir Abramovich:** Investigation, Validation. **Amit Agarwal:** Formal analysis, Data curation. **Maya Bar Sadan:** Supervision, Resources, Methodology. **Antonio Politano:** Supervision, Resources, Methodology, Conceptualization, Writing – review & editing. **Efrem Curcio:** Supervision, Resources, Methodology, Conceptualization, Writing – review & editing.

Declaration of competing interest

The authors declare the following financial interests/personal relationships which may be considered as potential competing interests: Maya Bar Sadan reports financial support was provided by Ministry of Science and Technology (MOST). Antonio Politano reports financial support was provided by Ministero degli Affari Esteri e della Cooperazione Internazionale (MAECI). Danil W. Boukhvalov reports financial support was provided by Jiangsu Innovative and Entrepreneurial Talents Project.

Data availability

Data will be made available on request.

Acknowledgments

AP and MBS acknowledge the IVANHOE project funded by the Ministero degli Affari Esteri e della Cooperazione Internazionale (MAECI) for Italy and Ministry of Science and Technology (MOST) for Israel. DWB acknowledges research funding from Jiangsu Innovative and Entrepreneurial Talents Project.

References

[1] I. Černý, M. Vaněk, E.W. Maruszewska, F. Beneš, How economic indicators impact the EU internal demand for critical raw materials, Resour. Policy. 74 (2021), 102417, https://doi.org/10.1016/j.resourpol.2021.102417.
[2] F.F. Martins, H. Castro, Raw material depletion and scenario assessment in European Union – a circular economy approach, Energy Rep. 6 (2020) 417–422, https://doi.org/10.1016/j.egyr.2019.08.082.
[3] S. Santoro, A.H. Avci, M. Aquino, L. Pugliese, S. Straface, E. Curcio, Towards the Global Rise of Zero Liquid Discharge for Wastewater Management: The Mining Industry Case in Chile, Springer Berlin Heidelberg, Berlin, Heidelberg, 2021, pp. 1–14, https://doi.org/10.1007/698_2021_785.
[4] S. Kalantzakos, The race for critical minerals in an era of geopolitical realignments, Int. Spect. 55 (2020) 1–16, https://doi.org/10.1080/03932729.2020.1786926.
[5] L. Dong, X. Tong, X. Li, J. Zhou, S. Wang, B. Liu, Some developments and new insights of environmental problems and deep mining strategy for cleaner production in mines, J. Clean. Prod. 210 (2019) 1562–1578, https://doi.org/10.1016/j.jclepro.2018.10.291.
[6] S. Santoro, H. Estay, A.H. Avci, L. Pugliese, R. Ruby-Figueroa, A. Garcia, M. Aquino, S. Nasirov, S. Straface, E. Curcio, Membrane technology for a sustainable copper mining industry: the Chilean paradigm, Clean. Eng. Technol. 2 (2021), 100091, https://doi.org/10.1016/j.clet.2021.100091.
[7] A. Upadhyay, T. Laing, V. Kumar, M. Dora, Exploring barriers and drivers to the implementation of circular economy practices in the mining industry, Resour. Policy. 72 (2021), 102037, https://doi.org/10.1016/j.resourpol.2021.102037.
[8] M.S. Diallo, M.R. Kotte, M. Cho, Mining critical metals and elements from seawater: opportunities and challenges, Environ. Sci. Technol. 49 (2015) 9390–9399, https://doi.org/10.1021/acs.est.5b00463.
[9] M.O. Mavukkandy, C.M. Chabib, I. Mustafa, A. Al Ghaferi, F. AlMarzooqi, Brine management in desalination industry: from waste to resources generation, Desalination. 472 (2019), 114187, https://doi.org/10.1016/j.desal.2019.114187.
[10] F. Macedonio, A. Criscuoli, L. Gzara, M. Albeirutty, E. Drioli, Water and salts recovery from desalination brines: An exergy evaluation, J. Environ. Chem. Eng. 9 (2021), 105884, https://doi.org/10.1016/j.jece.2021.105884.
[11] P. Loganathan, G. Naidu, S. Vigneswaran, Mining valuable minerals from seawater: a critical review, Environ. Sci. Water Res. Technol. 3 (2017) 37–53, https://doi.org/10.1039/c6ew00268d.
[12] E. Drioli, E. Curcio, A. Criscuoli, G. Di Di Profio, Integrated system for recovery of CaCO3, NaCl and MgSO 4·7H2O from nanofiltration retentate, J. Memb. Sci. 239 (2004) 27–38, https://doi.org/10.1016/j.memsci.2003.09.028.
[13] C.A. Quist-Jensen, F. Macedonio, E. Drioli, Membrane crystallization for salts recovery from brine—an experimental and theoretical analysis, Desalin. Water Treat. 57 (2016) 7593–7603, https://doi.org/10.1080/19443994.2015.1030110.
[14] A. Cerda, M. Quilaqueo, L. Barros, G. Seriche, M. Gim-Krumm, S. Santoro, A. H. Avci, J. Romero, E. Curcio, H. Estay, Recovering water from lithium-rich brines by a fractionation process based on membrane distillation-crystallization, J. Water Process Eng. 41 (2021), 102063, https://doi.org/10.1016/j.jwpe.2021.102063.
[15] M. Quilaqueo, G. Seriche, L. Barros, C. González, J. Romero, R. Ruby-Figueroa, S. Santoro, E. Curcio, H. Estay, Water recovery assessment from hypersaline lithium-rich brines using membrane distillation-crystallization, Desalination. 537 (2022), 115887, https://doi.org/10.1016/j.desal.2022.115887.
[16] P. Wang, T.-S. Chung, Recent advances in membrane distillation processes: membrane development, configuration design and application exploring, J. Memb. Sci. 474 (2015) 39–56, https://doi.org/10.1016/j.memsci.2014.09.016.
[17] S. Santoro, P. Timpano, A.H. Avci, P. Argurio, F. Chidichimo, M. De Biase, S. Straface, E. Curcio, An integrated membrane distillation, photocatalysis and polyelectrolyte-enhanced ultrafiltration process for arsenic remediation at point-of-use, Desalination. 520 (2021), 115378, https://doi.org/10.1016/j.desal.2021.115378.
[18] A. Ali, C.A. Quist-Jensen, F. Macedonio, E. Drioli, Application of membrane crystallization for minerals' recovery from produced water, Membranes (Basel). 5 (2015) 772–792, https://doi.org/10.3390/membranes5040772.
[19] E. Drioli, E. Curcio, A. Criscuoli, G. Di Profio, Integrated system for recovery of CaCO3, NaCl and MgSO4·7H2O from nanofiltration retentate, J. Memb. Sci. 239 (2004) 27–38, https://doi.org/10.1016/j.memsci.2003.09.028.
[20] B.K. Pramanik, K. Thangavadivel, L. Shu, V. Jegatheesan, A critical review of membrane crystallization for the purification of water and recovery of minerals, Rev. Environ. Sci. Bio/Technol. 15 (2016) 411–439, https://doi.org/10.1007/s11157-016-9403-0.
[21] E. Curcio, E. Fontananova, G. Di Profio, E. Drioli, Influence of the structural properties of poly(vinylidene fluoride) membranes on the heterogeneous nucleation rate of protein crystals, J. Phys. Chem. B 110 (2006) 12438–12445, https://doi.org/10.1021/jp061531y.
[22] E. Curcio, V. Curcio, G. Di Profio, E. Fontananova, E. Drioli, Energetics of protein nucleation on rough polymeric surfaces, J. Phys. Chem. B 114 (2010) 13650–13655, https://doi.org/10.1021/jp106349d.
[23] E. Curcio, V. López-Mejías, G. Di Profio, E. Fontananova, E. Drioli, B.L. Trout, A. S. Myerson, Regulating nucleation kinetics through molecular interactions at the polymer–solute interface, Cryst. Growth Des. 14 (2014) 678–686, https://doi.org/10.1021/cg4015543.
[24] G. Di Profio, E. Curcio, S. Ferraro, C. Stabile, E. Drioli, Effect of supersaturation control and heterogeneous nucleation on porous membrane surfaces in the crystallization of l-glutamic acid polymorphs, Cryst. Growth Des. 9 (2009) 2179–2186, https://doi.org/10.1021/cg800838b.
[25] S. Santoro, I. Vidorreta, I. Coelhoso, J.C. Lima, G. Desiderio, G. Lombardo, E. Drioli, R. Mallada, J. Crespo, A. Criscuoli, A. Figoli, Experimental evaluation of the thermal polarization in direct contact membrane distillation using electrospun nanofiber membranes doped with molecular probes, Molecules. 24 (2019) 638.
[26] S. Santoro, I.M. Vidorreta, V. Sebastian, A. Moro, I.M. Coelhoso, C.A.M. Portugal, J. C. Lima, G. Desiderio, G. Lombardo, E. Drioli, R. Mallada, J.G. Crespo, A. Criscuoli, A. Figoli, A non-invasive optical method for mapping temperature polarization in direct contact membrane distillation, J. Membr. Sci. 536 (2017) 156–166, https://doi.org/10.1016/j.memsci.2017.05.001.
[27] S.O. Olatunji, L.M. Camacho, Heat and mass transport in modeling membrane distillation configurations: a review, Front. Energy Res. 6 (2018) 130, https://doi.org/10.3389/fenrg.2018.00130.
[28] G. Zaragoza, A. Ruiz-Aguirre, E. Guillén-Burrieza, Efficiency in the use of solar thermal energy of small membrane desalination systems for decentralized water production, Appl. Energy 130 (2014) 491–499, https://doi.org/10.1016/j.apenergy.2014.02.024.
[29] M. Khayet, Solar desalination by membrane distillation: dispersion in energy consumption analysis and water production costs (a review), Desalination. 308 (2013) 89–101, https://doi.org/10.1016/j.desal.2012.07.010.
[30] A. Politano, P. Argurio, G. Di Profio, V. Sanna, A. Cupolillo, S. Chakraborty, H. A. Arafat, E. Curcio, Photothermal membrane distillation for seawater desalination, Adv. Mater. 29 (2017) 1603504, https://doi.org/10.1002/adma.201603504.
[31] A. Politano, G. Di Profio, E. Fontananova, V. Sanna, A. Cupolillo, E. Curcio, Overcoming temperature polarization in membrane distillation by thermoplasmonic effects activated by Ag nanofillers in polymeric membranes, Desalination. 451 (2019) 192–199, https://doi.org/10.1016/j.desal.2018.03.006.
[32] S. Santoro, A.H. Avci, A. Politano, E. Curcio, The advent of thermoplasmonic membrane distillation, Chem. Soc. Rev. 51 (2022) 6087–6125, https://doi.org/10.1039/D0CS00097C.
[33] A.H. Avci, S. Santoro, A. Politano, M. Propato, M. Micieli, M. Aquino, Z. Wenjuan, E. Curcio, Photothermal sweeping gas membrane distillation and reverse electrodialysis for light-to-heat-to-power conversion, Chem. Eng. Process. - Process Intensif. (2021), 108382, https://doi.org/10.1016/j.cep.2021.108382.
[34] J. Wu, K.R. Zodrow, P.B. Szemraj, Q. Li, Photothermal nanocomposite membranes for direct solar membrane distillation, J. Mater. Chem. A 5 (2017) 23712–23719, https://doi.org/10.1039/C7TA04555G.
[35] P.D. Dongare, A. Alabastri, S. Pedersen, K.R. Zodrow, N.J. Hogan, O. Neumann, J. Wu, T. Wang, A. Deshmukh, M. Elimelech, Q. Li, P. Nordlander, N.J. Halas, Nanophotonics-enabled solar membrane distillation for off-grid water purification, Proc. Natl. Acad. Sci. 114 (2017) 6936–6941, https://doi.org/10.1073/pnas.1701835114.

[36] J. Huang, Y. Hu, Y. Bai, Y. He, J. Zhu, Novel solar membrane distillation enabled by a PDMS/CNT/PVDF membrane with localized heating, Desalination. 489 (2020), 114529, https://doi.org/10.1016/j.desal.2020.114529.
[37] S. Santoro, M. Aquino, D. Han Seo, T. Van Der Laan, M. Lee, J. Sung Yun, M. Jun Park, A. Bendavid, H. Kyong Shon, A. Halil Avci, E. Curcio, Dimensionally controlled graphene-based surfaces for photothermal membrane crystallization, J. Colloid Interface Sci. (2022), https://doi.org/10.1016/j.jcis.2022.05.062.
[38] A. Politano, G. Chiarello, Plasmon modes in graphene: status and prospect, Nanoscale. 6 (2014) 10927–10940, https://doi.org/10.1039/C4NR03143A.
[39] S. Santoro, M. Aquino, C. Rizza, J. Occhiuzzi, D. Mastrippolito, G. D'Olimpio, A. H. Avci, J. De Santis, V. Paolucci, L. Ottaviano, L. Lozzi, A. Ronen, M. Bar-Sadan, D. S. Han, A. Politano, E. Curcio, Lithium recovery through WS2 nanofillers-promoted solar photothermal membrane crystallization of LiCl, Desalination. 546 (2023), 116186, https://doi.org/10.1016/j.desal.2022.116186.
[40] A.H. Avci, S. Santoro, A. Politano, M. Propato, M. Micieli, M. Aquino, Z. Wenjuan, E. Curcio, Photothermal sweeping gas membrane distillation and reverse electrodialysis for light-to-heat-to-power conversion, Chem. Eng. Process. - Process Intensif. 164 (2021), 108382, https://doi.org/10.1016/j.cep.2021.108382.
[41] S. Abramovich, D. Dutta, C. Rizza, S. Santoro, M. Aquino, A. Cupolillo, J. Occhiuzzi, M.F. La Russa, B. Ghosh, D. Farias, A. Locatelli, D.W. Boukhvalov, A. Agarwal, E. Curcio, M. Bar Sadan, A. Politano, NiSe and CoSe topological nodal-line semimetals: a sustainable platform for efficient thermoplasmonics and solar-driven photothermal membrane distillation, Small. 18 (2022) 2201473, https://doi.org/10.1002/smll.202201473.
[42] A. Lalisse, G. Tessier, J. Plain, G. Baffou, Quantifying the efficiency of plasmonic materials for near-field enhancement and photothermal conversion, J. Phys. Chem. C 119 (2015) 25518–25528, https://doi.org/10.1021/acs.jpcc.5b09294.
[43] S. Santoro, V. Sebastian, A.J. Moro, C.A.M. Portugal, J.C. Lima, I.M. Coelhoso, J. G. Crespo, R. Mallada, Development of fluorescent thermoresponsive nanoparticles for temperature monitoring on membrane surfaces, J. Colloid Interface Sci. 486 (2017) 144–152, https://doi.org/10.1016/j.jcis.2016.09.059.
[44] J. Garside, A. Mersmann, J. Nyvlt, Measurement of Crystal Growth and Nucleation Rates, 2d Ed, IChemE, Rudby, 2002.
[45] X. Wu, G.Y. Chen, G. Owens, D. Chu, H. Xu, Photothermal materials: a key platform enabling highly efficient water evaporation driven by solar energy, Mater. Today, Energy. 12 (2019) 277–296, https://doi.org/10.1016/j.mtener.2019.02.001.
[46] A. Mersmann, M. Angerhöfer, T. Gutwald, R. Sangl, S. Wang, General prediction of median crystal sizes, Sep. Technol. 2 (1992) 85–97, https://doi.org/10.1016/0956-9618(92)80011-2.
[47] W. Hu, W. Zhen, M. Zhang, W. Wang, X. Jia, S. An, Y. Wang, Z. Guo, X. Jiang, Development of nickel selenide@polydopamine nanocomposites for magnetic resonance imaging guided NIR-II photothermal therapy, Adv. Healthc. Mater. 10 (2021) 2101542, https://doi.org/10.1002/adhm.202101542.
[48] B. Ung, Y. Sheng, Interference of surface waves in a metallic nanoslit, Opt. Express 15 (2007) 1182–1190, https://doi.org/10.1364/oe.15.001182.
[49] D. Rana, T. Matsuura, C.Q. Lan, Work needed to force the water-air interface down in the re-entrant structured capillary pore, Desalination. 541 (2022), 116058, https://doi.org/10.1016/j.desal.2022.116058.
[50] H. Chamani, T. Matsuura, D. Rana, C.Q. Lan, Transport characteristics of liquid-gas interface in a capillary membrane pore, J. Memb. Sci. 611 (2020), 118387, https://doi.org/10.1016/j.memsci.2020.118387.
[51] D. Rana, B.M. Mandal, S.N. Bhattacharyya, Analogue calorimetry of polymer blends: poly(styrene-co-acrylonitrile) and poly(phenyl acrylate) or poly(vinyl benzoate), Polymer (Guildf). 37 (1996) 2439–2443, https://doi.org/10.1016/0032-3861(96)85356-0.
[52] C. Bhattacharya, N. Maiti, B.M. Mandal, S.N. Bhattacharyya, Thermodynamic characterization of miscible blends from very similar polymers by inverse gas chromatography. The poly(ethyl acrylate)-poly(vinyl propionate) system, Macromolecules. 22 (1989) 4062–4068, https://doi.org/10.1021/ma00200a043.
[53] M. Qtaishat, T. Matsuura, B. Kruczek, M. Khayet, Heat and mass transfer analysis in direct contact membrane distillation, Desalination. 219 (2008) 272–292, https://doi.org/10.1016/j.desal.2007.05.019.
[54] M. Gryta, M. Tomaszewska, Heat transport in the membrane distillation process, J. Memb. Sci. 144 (1998) 211–222, https://doi.org/10.1016/S0376-7388(98)00050-7.
[55] P. Patnaik, Handbook of Inorganic Chemicals, McGraw-Hill, New York, 2003.
[56] M.-C. Sparenberg, S. Chergaoui, V. Sang Sefidi, P. Luis, Crystallization control via membrane distillation-crystallization: A review, Desalination. 519 (2021), 115315, https://doi.org/10.1016/j.desal.2021.115315.
[57] E. Drioli, G. Di Profio, E. Curcio, Membrane-Assisted Crystallization Technology, Imperial College Press, 2015, https://doi.org/10.1142/p912.
[58] B. der Bruggen, Nucleation stage crystal growth, in: E. Drioli, L. Giorno (Eds.), Encycl. Membr, Springer, Berlin Heidelberg, Berlin, Heidelberg, 2015, pp. 1–2, https://doi.org/10.1007/978-3-642-40872-4_417-1.
[59] G. Di Profio, E. Curcio, E. Drioli, Supersaturation control and heterogeneous nucleation in membrane crystallizers: facts and perspectives, Ind. Eng. Chem. Res. 49 (2010) 11878–11889, https://doi.org/10.1021/ie100418z.
[60] S. Santoro, R.A. Tufa, A.H. Avci, E. Fontananova, G. Di Profio, E. Curcio, Fouling propensity in reverse electrodialysis operated with hypersaline brine, Energy (2021) 120563, https://doi.org/10.1016/j.energy.2021.120563.
[61] J. Kim, J. Kim, S. Hong, Recovery of water and minerals from shale gas produced water by membrane distillation crystallization, Water Res. 129 (2018) 447–459, https://doi.org/10.1016/j.watres.2017.11.017.
[62] X. Ji, E. Curcio, S. Al Obaidani, G. Di Profio, E. Fontananova, E. Drioli, Membrane distillation-crystallization of seawater reverse osmosis brines, Sep. Purif. Technol. 71 (2010) 76–82, https://doi.org/10.1016/j.seppur.2009.11.004.
[63] A.J. Asselberg, Evaporating Crystallizers: A Study of Factors in Operation and Design of Salt Evaporators, Delft Technical University, 1978.
[64] R. Molinari, A.H. Avci, P. Argurio, E. Curcio, S. Meca, M. Plà-Castellana, J. L. Cortina, Selective precipitation of calcium ion from seawater desalination reverse osmosis brine, J. Clean. Prod. 328 (2021), 129645, https://doi.org/10.1016/j.jclepro.2021.129645.